

Monte Carlo simulations of clinical PET and SPECT scans: impact of the input data on the simulated images

This article has been downloaded from IOPscience. Please scroll down to see the full text article.

2011 Phys. Med. Biol. 56 6441

(<http://iopscience.iop.org/0031-9155/56/19/017>)

View [the table of contents for this issue](#), or go to the [journal homepage](#) for more

Download details:

IP Address: 132.166.112.37

The article was downloaded on 30/09/2011 at 11:26

Please note that [terms and conditions apply](#).

Monte Carlo simulations of clinical PET and SPECT scans: impact of the input data on the simulated images

S Stute¹, T Carlier², K Cristina¹, C Noblet², A Martineau³, B Hutton⁴,
L Barnden⁴ and I Buvat¹

¹ IMNC—UMR 8165 CNRS—Paris 7 and Paris 11 Universities, 15 rue Georges Clémenceau, 91406 Orsay Cedex, France

² INSERM U892—Cancer Research Center, University of Nantes and Nuclear Medicine Department, University Hospital of Nantes, Nantes, France

³ Department of Nuclear Medicine, Saint-Louis Hospital, Paris, France

⁴ Institute of Nuclear Medicine, UCL, London, UK

E-mail: stute@imnc.in2p3.fr

Received 16 March 2011, in final form 3 August 2011

Published 20 September 2011

Online at stacks.iop.org/PMB/56/6441

Abstract

Monte Carlo simulations of emission tomography have proven useful to assist detector design and optimize acquisition and processing protocols. The more realistic the simulations, the more straightforward the extrapolation of conclusions to clinical situations. In emission tomography, accurate numerical models of tomographs have been described and well validated under specific operating conditions (collimator, radionuclide, acquisition parameters, count rates, etc). When using these models under these operating conditions, the realism of simulations mostly depends on the activity distribution used as an input for the simulations. It has been proposed to derive the input activity distribution directly from reconstructed clinical images, so as to properly model the heterogeneity of the activity distribution between and within organs. However, reconstructed patient images include noise and have limited spatial resolution. In this study, we analyse the properties of the simulated images as a function of the properties of the reconstructed images used to define the input activity distributions in ¹⁸F-FDG PET and ¹³¹I SPECT simulations. The propagation through the simulation/reconstruction process of the noise and spatial resolution in the input activity distribution was studied using simulations. We found that the noise properties of the images reconstructed from the simulated data were almost independent of the noise in the input activity distribution. The spatial resolution in the images reconstructed from the simulations was slightly poorer than that in the input activity distribution. However, using high-noise but high-resolution patient images as an input activity distribution yielded reconstructed images that could not be distinguished from clinical images. These findings were confirmed by

simulated highly realistic ^{131}I SPECT and ^{18}F -FDG PET images from patient data. In conclusion, we demonstrated that ^{131}I SPECT and ^{18}F -FDG PET images indistinguishable from real scans can be simulated using activity maps with spatial resolution higher than that used in routine clinical applications.

(Some figures in this article are in colour only in the electronic version)

1. Introduction

Monte Carlo (MC) simulations of positron emission tomography (PET) and single-photon emission computed tomography (SPECT) are extremely useful to assist detector design and optimize imaging and processing protocols. The more realistic the simulations of SPECT and PET images, the more straightforward the extrapolation of conclusions obtained from the simulated data to the clinical settings. We have recently proposed an efficient method to model highly realistic patient PET scans (Stute *et al* 2008). The method has been extended to model highly realistic patient SPECT scans (Carlier *et al* 2009). In this approach, the activity and attenuation maps needed to define the simulation input are derived from real PET or SPECT and x-ray computed tomography (CT) scans of patients. By doing so, the intrinsic heterogeneity of the activity distribution between and within organs can be accurately modelled. This is a definite advantage compared to the more conventional approach consisting in modelling a piece-wise constant activity map based on an anthropomorphic phantom (Segars and Tsui 2009) and manual measurements in real PET images (Le Maitre *et al* 2009, Tomei *et al* 2010). However, the drawback associated with the use of patient images to define the activity map serving as an input for MC simulations is that the patient images suffer from limited spatial resolution and noise. The limited spatial resolution and noise propagate through the simulation and reconstruction processes, which might result in simulated images substantially different from those obtained in the clinics. The aim of the work described in this paper was to investigate how the spatial resolution and noise in the patient images used as an input for MC simulations impact the images reconstructed from the simulated data. The study was carried out for both SPECT and PET images, so as to derive recommendations appropriate for performing MC simulations of SPECT and PET images based on real PET/CT or SPECT/CT data.

The organization of the paper is as follows: in section 2, we describe the method used to study the propagation of the limited spatial resolution and noise characterizing the input data of the MC simulation through the simulation/reconstruction process. Section 3 presents the results in the PET and SPECT cases. Section 4 discusses the results and derives some recommendations to simulate highly realistic images from real PET/CT or SPECT/CT images.

2. Methods

To study the propagation of noise or limited spatial resolution in the input activity map through the simulation and reconstruction processes, we generated activity maps corresponding to a broad range of noise magnitudes and spatial resolutions. Simulations were performed to derive the corresponding SPECT and PET sinograms. Finally, SPECT or PET images were reconstructed from these sinograms. The noise and spatial resolution in the reconstructed images were then characterized and compared to those of the input activity maps. The goal was to determine which noise and spatial resolution in the input activity maps led to reconstructed

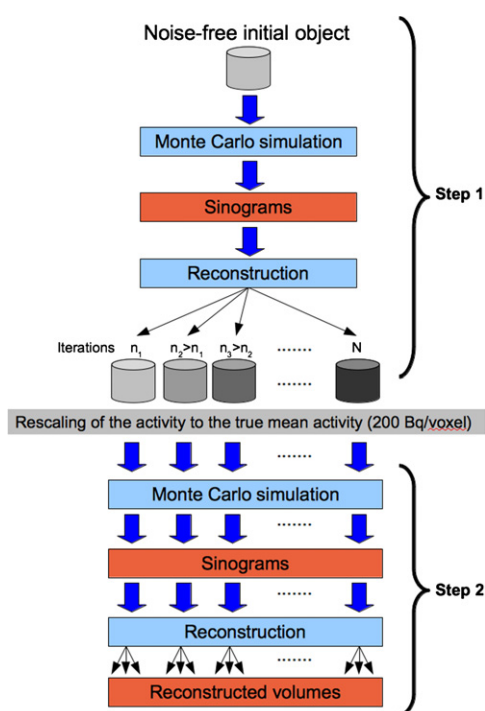


Figure 1. Flowchart of the noise propagation study for a cylinder with uniform activity. Each thin arrow represents an iterative reconstruction process with a specific number of iteration.

images with noise and spatial resolution matching those observed in real clinical data. In this work, we only considered iterative reconstruction and all simulations were performed within the GATE (Geant4 Application in Emission Tomography) platform (Jan *et al* 2004, 2011). The fictitious interaction tracking algorithm (Rehfeld *et al* 2009) was used to speed up the MC computation, as well as the angular response function option (Descourt *et al* 2010) for the SPECT simulations.

2.1. Effect of the noise present in the input activity map

To model the correlated noise present in real PET or SPECT images, we simulated PET and SPECT sinograms from a noise-free uniform activity distribution and reconstructed the corresponding images. Using reconstructed images corresponding to different numbers of iterations gave images with different noise levels (this first step is hereafter denoted as ‘step 1’). The resulting so-called INPUT images were first multiplied by a constant so that the mean signal was equal to the true signal of the noise-free activity distribution. The resulting images were then used as an input for simulating new images mimicking those that would be obtained when using real reconstructed images as input activity maps (denoted hereafter as ‘step 2’). Figure 1 illustrates the principle of the noise propagation study. The noise in the OUTPUT images reconstructed with various numbers of iterations from the step 2 simulation was then compared to the noise in the INPUT images, to characterize the propagation of the noise.

2.1.1. Simulations and reconstructions. A cylinder filled with uniform activity was considered. Its dimensions were 18 cm in length and 20 cm in diameter for the PET case, and 18.6 cm in length and 21.6 cm in diameter for the SPECT case. The sampling of the object was $124 \times 124 \times 45$ voxels of $4 \times 4 \times 4$ mm³ in PET and $128 \times 128 \times 39$ voxels of $4.8 \times 4.8 \times 4.8$ mm³ in SPECT. An activity of 200 Bq per voxel was set in the cylinder (¹⁸F for PET and ¹³¹I for SPECT).

In PET, the GEMINI GXL scanner (Philips Healthcare) was modelled (Lamare *et al* 2006). Acquisitions of 120 s duration were considered (one bed position only). Annihilations were simulated (positron range and non-colinearity were not modelled). Events from the normal and delayed coincidence windows were recorded in raw non-compressed and non-interpolated sinograms (Kadrmas 2004). Scatter sinograms were estimated using a convolution–subtraction method (Bailey and Meikle 1994). The sinogram of the attenuation correction factors was calculated by forward-projecting an image of the cylinder ($4 \times 4 \times 4$ mm³ voxel sampling), containing the same attenuation coefficients as those used in the simulations. Images of $144 \times 144 \times 45$ voxels of $4 \times 4 \times 4$ mm³ were finally reconstructed using a home-made OP-OSEM algorithm (Politte and Snyder 1991), which includes the random and scatter corrections in the iterative loop, and uses a weighted attenuation correction. The Siddon (1985) projector was implemented. Ten subsets were used for steps 1 and 2, and images corresponding to 10, 20, 40, 70, 100, 150, 200, 300, 500 and 1000 equivalent MLEM iterations were stored. No post-filtering was applied.

Given that in PET the sensitivity, hence the noise level, varies along the scanner axis, 45 replicates from step 1 were generated and only the central transaxial slice from each reconstructed image volume was subsequently used. These slices were then stacked up to build the INPUT activity distribution for step 2. Using this approach, the INPUT noise level of the activity distribution was axially invariant. Generating multiple replicates consisted in running exactly the same MC simulation but using a different seed in the generator of pseudo-random numbers for each replicate. Each replicate was then reconstructed independently following the procedure described above.

In SPECT, a model of the Siemens SYMBIA T equipped with a high-energy collimator (8000 holes, hole diameter: 4 mm, septal thickness: 2 mm, hole length: 59.5 mm) was considered. Acquisitions of 64 projections of 30 s each (matrix size: 128×128 , pixel size: 4.8×4.8 mm²) were simulated, with a radius of rotation of 28 cm. The system spatial resolution measured in a planar acquisition at 28 cm from the collimator was 27 mm full-width at half-maximum (FWHM). The Flash3D software developed by Siemens incorporating a fast OSEM reconstruction with attenuation and 3D resolution modelling (Vija *et al* 2004) was used. Volumes were reconstructed with a sampling of $128 \times 128 \times 39$ (voxel size: $4.8 \times 4.8 \times 4.8$ mm³). Eight subsets were used in the OSEM reconstruction for steps 1 and 2, and images corresponding to 16, 40, 80, 120, 160, 200, 240 and 480 equivalent MLEM iterations (the latter being the maximum permitted by the software) were stored. No post-filtering was applied.

2.1.2. Figures of merit for noise characterization.

Noise level measurement. Ideally, a precise noise characterization requires the simulation of many replicates for a given configuration, to derive the variance image (Barrett *et al* 1994, Schmidtlein *et al* 2010, Tong *et al* 2010). In our study, this was impractical as we wanted to investigate several different input noise levels in the simulations, implying the generation of replicates for both step 1 and step 2. We thus used a different figure of merit (FOM) to

measure the noise from a single replicate. This FOM was first validated against the reference FOM based on multiple replicates of step 1. The reference noise FOM B_j , in a voxel j of a given slice, is defined by

$$B_j = \frac{\sigma_j}{m_j} \times 100 \quad \text{where} \quad m_j = \frac{1}{K} \sum_{k=1}^K f_j^k, \sigma_j = \sqrt{\frac{1}{K} \sum_{k=1}^K (m_j - f_j^k)^2} \quad (1)$$

Here, m_j and σ_j are the mean and standard deviation of voxel j through the K replicates of the reconstructed images f^k , respectively. To get better statistics, B_j was measured in J different uncorrelated voxels inside the same slice of the cylinder, and a noise FOM B (called PIXEL noise hereafter) was defined by

$$B = \frac{1}{J} \sum_{j=1}^J B_j \quad (2)$$

The proposed noise FOM \hat{B}_r measured inside a given region of interest (ROI) R_r of V voxels from a unique replicate was defined by

$$\hat{B}_r = \frac{\hat{\sigma}_r}{\hat{m}_r} \times 100 \quad \text{where} \quad \hat{m}_r = \frac{1}{V} \sum_{j \in R_r} f_j, \quad \hat{\sigma}_r = \sqrt{\frac{1}{V} \sum_{j \in R_r} (\hat{m}_r - f_j)^2} \quad (3)$$

Here, \hat{m}_r and $\hat{\sigma}_r$ are the mean and standard deviation in the V voxels of ROI R_r in the reconstructed image f , respectively. \hat{B}_r was measured in R ROIs contained in the cylinder, and a noise FOM \hat{B} (called ROI noise hereafter) was defined as

$$\hat{B} = \frac{1}{R} \sum_{r=1}^R \hat{B}_r. \quad (4)$$

Each ROI consisted in a number V of voxels, where V was equal to the number of replicates used to calculate the reference FOM ($V = K$). Also, the reference FOM was measured in a given number of voxels, equal to the number of ROIs considered in the proposed FOM ($R = J$). The proposed FOM was validated in step 1, using all stored iterations. In PET, we used the previously simulated $K = 45$ replicates, and in SPECT, $K = 32$ replicates were simulated, while in both cases $R = J = 10$. In PET, the sensitivity, hence the noise, varies along the axial direction. Therefore, we restricted our study to the central slice for both PET and SPECT. The R ROIs were randomly chosen, in such a way that they were distant by at least two voxels from each other and three voxels from the cylinder's border. The $R = 10$ ROIs obtained for the PET study are shown in figure 2. The J pixels were chosen at the centre of each ROI.

Noise level propagation. In all configurations, the proposed FOM was used to measure the noise level. For several output iterations of step 1, the noise level was measured. Each of these noise levels corresponded to an INPUT noise in step 2. Then, for all step 2 simulations, the OUTPUT noise level in the images was measured for several iteration numbers. Finally, these OUTPUT noise levels were plotted against the INPUT noise.

Noise correlation propagation. To calculate the noise correlation, many replicates of the same simulation are needed. The noise correlation in images from step 1 was first calculated using the K replicates that were simulated to perform the validation of the proposed FOM \hat{B} against the reference FOM B . This noise correlation thus represented the reference, corresponding to noise-free INPUT images. Then, for the PET (resp. SPECT) case, 45 (resp. 32) replicates

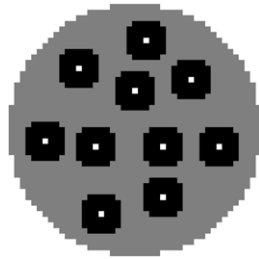


Figure 2. Transaxial slice across the ideal PET cylinder (in grey) and the $R = 10$ randomly chosen ROIs (in black). The $J = 10$ voxels associated with the reference FOM are at the centre of each ROI (in white). The voxel size in the image shown here is the same as in the reconstructed PET images.

of step 2 were simulated for two different INPUT noise levels (calculated with the proposed FOM): 51% and 89% in PET corresponding to 50 and 600 MLEM iterations (5 and 60 using ten subsets), and 3.5% and 7.9% in SPECT, corresponding to 40 and 200 MLEM iterations (5 and 25 using eight subsets). The first noise level is close to the one in clinical images, before post-smoothing. The second one was chosen to represent a higher level of noise.

We calculated the correlation $C_{i,j}$ between the noise of a voxel i at the centre of the cylinder on the central axial slice and the noise of all other voxels j within that same slice using

$$C_{i,j} = \frac{\frac{1}{K} \sum_{k=1}^K (m_i - f_i^k)(m_j - f_j^k)}{\sigma_i \sigma_j}. \quad (5)$$

Two-dimensional correlation images were created and profiles across these images were drawn. For any INPUT noise from which we calculated the OUTPUT noise correlation, the OUTPUT MLEM iteration considered was 600 for PET (60 iterations using 10 subsets) and 480 for SPECT (30 iterations using 16 subsets).

2.2. Effect of the spatial resolution in the input activity map

The impact of the spatial resolution in the INPUT activity map on the spatial resolution in the OUTPUT reconstructed images was studied by using INPUT activity maps corresponding to noise-free point sources blurred with different Gaussian point spread functions. The imaging of each point source was then simulated, and the OUTPUT images were reconstructed from the simulated sinograms.

The point sources in the reconstructed images were then fit using 2D Gaussian functions to determine the spatial resolution in the OUTPUT image as a function of the spatial resolution in the INPUT image.

2.2.1. Simulations and reconstructions. A noise-free point source, represented as a unique non-zero voxel, was placed in the central slice and approximately at 14 mm from the FOV centre in PET. In SPECT, the point source was centred in the FOV. This point source was blurred with 3D isotropic Gaussian functions with FWHM ranging from 1 to 40 mm. The INPUT matrix size was $490 \times 490 \times 179$ voxels of $1 \times 1 \times 1 \text{ mm}^3$ in PET, and $200 \times 200 \times 199$ voxels of $1.2 \times 1.2 \times 1.2 \text{ mm}^3$ in SPECT. In PET, acquisitions of 120 s were considered with a total activity of 10 MBq (for FWHM = 1 mm). Annihilations were simulated (positron range and non-collinearity were not modelled). In SPECT, 64 projections (matrix size:

256×256 , pixel size: $2.4 \times 2.4 \text{ mm}^2$) of 125 s were simulated with a total ^{131}I activity of 12 MBq (for FWHM = 1 mm). For higher INPUT FWHMs, the total activity of the blurred point source was successively increased in order to preserve a sufficient level of signal in the sinograms.

The simulated tomographs and the reconstruction algorithms were the same as for the noise propagation study, except the reconstructed volume size that was set to $192 \times 192 \times 60$ voxels of $3 \times 3 \times 3 \text{ mm}^3$ in PET and $256 \times 256 \times 163$ voxels of $2.4 \times 2.4 \times 2.4 \text{ mm}^3$ in SPECT.

2.2.2. FOM for characterizing spatial resolution. For both PET and SPECT studies, the convergence of the solution was first checked by fitting a 2D transaxial Gaussian to the OUTPUT reconstructed images and deriving the FWHM. It was assumed that the convergence was reached when the variation between successive FWHM values was less than 1%. The FWHM of the OUTPUT images was then plotted as a function of the FWHM in the INPUT images. After applying the Gaussian smoothing kernels to the point sources, the FWHM of the INPUT images was measured using the same methodology as for the OUTPUT images. Yet, as the voxel size is smaller in the INPUT images than in the OUTPUT images, a small discrepancy might exist between the INPUT and OUTPUT FWHM measurements.

2.3. Validation using simulations of real patient scans

To illustrate the validity of findings derived from simple phantom experiments, we simulated a PET and a SPECT scan from real patient data. Using the images reconstructed from the simulated data, we checked the impact of the noise and spatial resolution in the INPUT data on the noise and spatial resolution in the OUTPUT data and compared the results with the conclusions obtained on the phantom studies.

2.3.1. PET case. A patient was injected with 334 MBq of ^{18}F -FDG and scanned 1 h after injection. The reconstructed PET and CT images ($4 \times 4 \times 4 \text{ mm}^3$ sampling) were considered to define the INPUT activity and attenuation distribution of the GATE simulations. To define the attenuation distribution, the CT image was segmented in 23 different materials, from lung to high-density bones. The model of the Philips GEMINI GXL was used, and acquisitions of 120 s per bed positions (total of 5) were simulated. No lesions were seen in this patient. Annihilations were simulated (positron range and non-colinearity were not modelled).

Three different reconstructions of the original data were considered to define three activity maps. A 'clinical-like' reconstruction was used to get a low-noise but low-resolution INPUT image ($R_L N_L$), a highly iterated but post-filtered image was used to get a medium-noise and medium-resolution ($R_M N_M$) activity map, and finally a highly iterated image without post-filtering was used to get a high-noise and high-resolution ($R_H N_H$) activity map. All associated reconstruction parameters are given in table 1.

As the aim was to produce realistic clinical images, the acquired and simulated sinograms were reconstructed using parameters used in routine clinical practice (parameters corresponding to the $R_L N_L$ situation). Profiles were drawn through the clinical and simulated images.

2.3.2. SPECT case. The SPECT acquisition of a patient treated for a hepatocellular carcinoma with an intra-arterial injection of 2.2 GBq ^{131}I -iodized oil (Lipiodis[®]) was simulated. Real SPECT/CT acquisitions were performed seven days after injection. The reconstructed

Table 1. Reconstruction parameters of the original PET data used to produce the three different INPUT activity maps. Representative images are also shown.

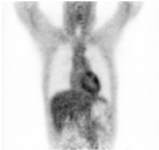


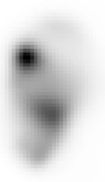


Input activity map	$R_L N_L$ ('low noise–low resolution')	$R_M N_M$ ('medium noise–medium resolution')	$R_H N_H$ ('high noise–high resolution')
Reconstruction set-up	32 MLEM iterations Attenuation, scatter and randoms correction using the OP model (Politte and Snyder 1991) 6 mm 3D Gaussian post-smoothing	1000 MLEM iterations Attenuation, scatter and randoms correction using the OP model (Politte and Snyder 1991) 6 mm 3D Gaussian post-smoothing	1000 MLEM iterations Attenuation, scatter and randoms correction using the OP model (Politte and Snyder 1991) No post-smoothing
Coronal section			

Table 2. Reconstruction parameters of the original SPECT data used to produce the three different INPUT activity maps. Representative images are also shown.

Input activity map	$R_L N_L$ ('low noise–low resolution')	$R_M N_M$ ('medium noise–medium resolution')	$R_H N_H$ ('high noise–high resolution')
Reconstruction set-up	30 MLEM iterations Attenuation correction 3D resolution modelling No post-smoothing	480 MLEM iterations Attenuation correction 3D resolution modelling 10 mm 3D Gaussian post-smoothing	480 MLEM iterations Attenuation correction 3D resolution modelling No post-smoothing
Coronal section			

SPECT and CT images ($4.8 \times 4.8 \times 4.8$ mm³ sampling) were used to define the INPUT activity and attenuation maps for the GATE simulations. To define the attenuation map, the CT image was segmented in three different materials (air, water and bone). The simulations mimicked an acquisition of 64 projections over 360° using the Siemens Symbia T camera.

Three different reconstructions using the Flash3D algorithm were considered to produce the INPUT activity maps (table 2). Each sinogram (one acquired and three simulated) was then reconstructed with the Flash3D algorithm (eight iterations, eight subsets, attenuation correction, 3D resolution modelling, 5 mm FWHM 3D Gaussian post-smoothing). Profiles across the reconstructed images were drawn to compare the simulated and real images.

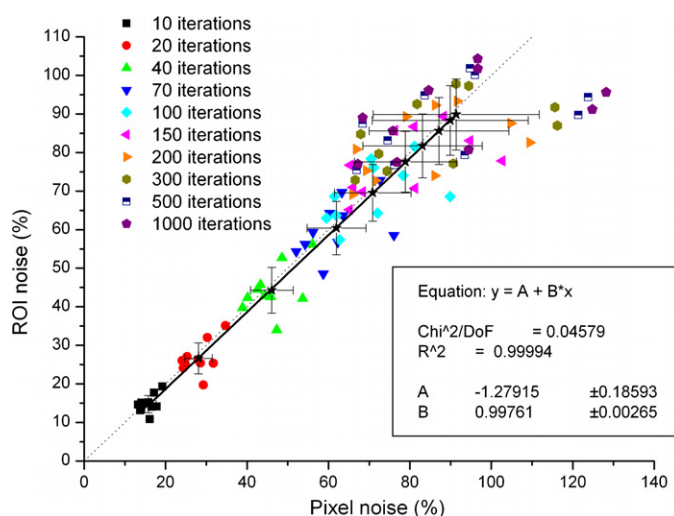


Figure 3. PIXEL noise (=reference FOM) against ROI noise (=proposed FOM) obtained in the PET simulations. The noise varies with the number of iterations. Each symbol represents a single PIXEL against its associated ROI (see figure 2) for a given iteration number. Black stars show the mean of each group of ten ROIs for each iteration number. The dotted line is the identity line. The thick line corresponds to a linear fit of the black stars.

3. Results

3.1. Effect of the noise present in the input activity map

The two noise FOMs are compared in figures 3 and 4 for the PET and SPECT cases. A high correlation was found between the proposed and reference FOMs. This showed the validity of the proposed FOM, based on a single noisy image, for the study regarding the noise propagation through the simulation process.

The impact of noise present in the INPUT activity map is illustrated in figure 5 for the PET and SPECT cases for different numbers of iterations after step 2. For 'low' INPUT noise values (typically less than 60% in PET and less than 6% in SPECT), there is a relationship between INPUT noise magnitude and OUTPUT noise magnitude: the higher the noise in the INPUT activity map, the higher the noise in the OUTPUT reconstructed image. However, from a certain level of INPUT noise (greater than 60% in PET and greater than 6% in SPECT), this relationship gets much weaker, and the OUTPUT noise is relatively constant irrespective of the INPUT noise.

The noise correlation images for the central pixel and profiles drawn across these images are shown in figure 6 for the PET and SPECT cases. The SPECT correlation images are much smoother than the PET correlation images. This is due to the 3D resolution modelling included in the Flash3D algorithm, as it is known that resolution modelling in the system matrix used for the reconstruction leads to broader correlation peaks (Sureau *et al* 2008, Stute *et al* 2011). In both SPECT and PET cases however, the correlation images are almost independent of the INPUT noise.

3.2. Effect of the spatial resolution in the input activity map

Figure 7 shows the convergence of the FWHM calculated in the reconstructed volumes for different values of the INPUT spatial resolution. In the PET case, the convergence was rapidly

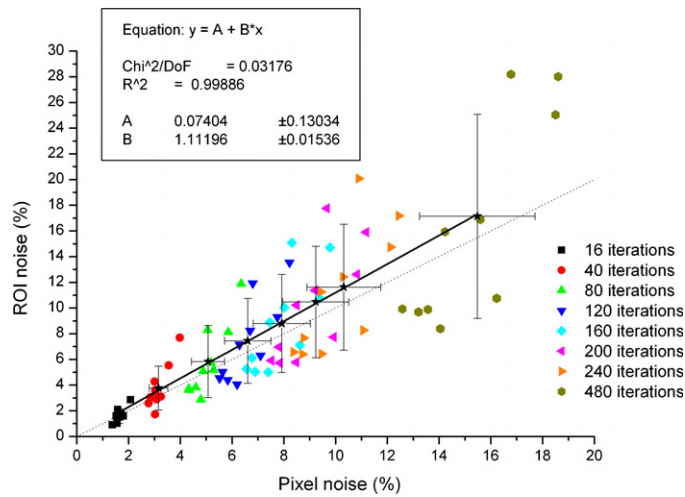


Figure 4. PIXEL noise (=reference FOM) against ROI noise (=proposed FOM) obtained in the SPECT simulations. The noise varies with the number of iterations. Each symbol represents a single PIXEL against its associated ROI (see figure 2) for a given iteration number. Black stars show the mean of each group of 10 ROIs for each iteration number. The dotted line is the identity line. The thick line corresponds to a linear fit of the black stars. Note that no more than 30 iterations and 16 subsets (i.e. 480 MLEM iterations) could be performed with the Flash3D algorithm as implemented in the console.

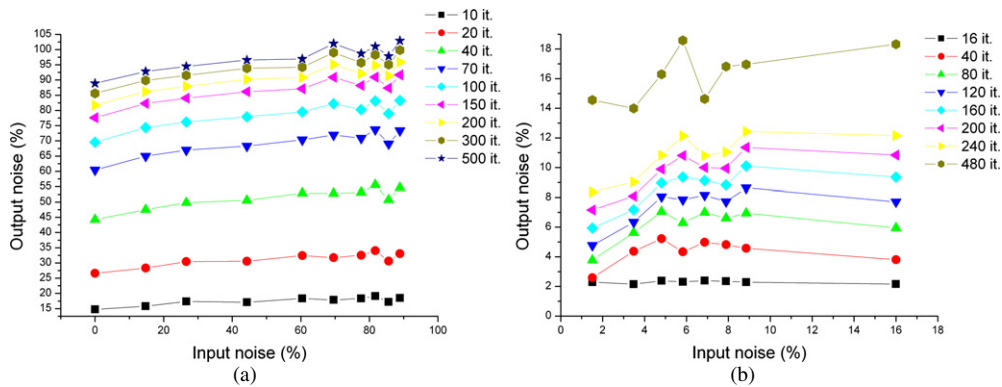


Figure 5. OUTPUT noise as a function of the INPUT noise for different OUTPUT iteration numbers in PET (a) and SPECT (b).

reached whatever the INPUT spatial resolution. In SPECT, our criterion of convergence was not reached due to the limited number of iterations possible with the Flash3D algorithm. All subsequent reconstructions were thus performed with the maximum number of iterations possible with the Flash3D algorithm (30 iterations and 16 subsets).

The OUTPUT spatial resolution is plotted as a function of the INPUT spatial resolution in figure 8. The OUTPUT spatial resolution tends to be identical to the INPUT spatial resolution from 10 mm spatial resolution in SPECT and 15 mm in PET. For INPUT spatial resolution below 10 mm, reconstructed spatial resolution was better in SPECT than in PET.

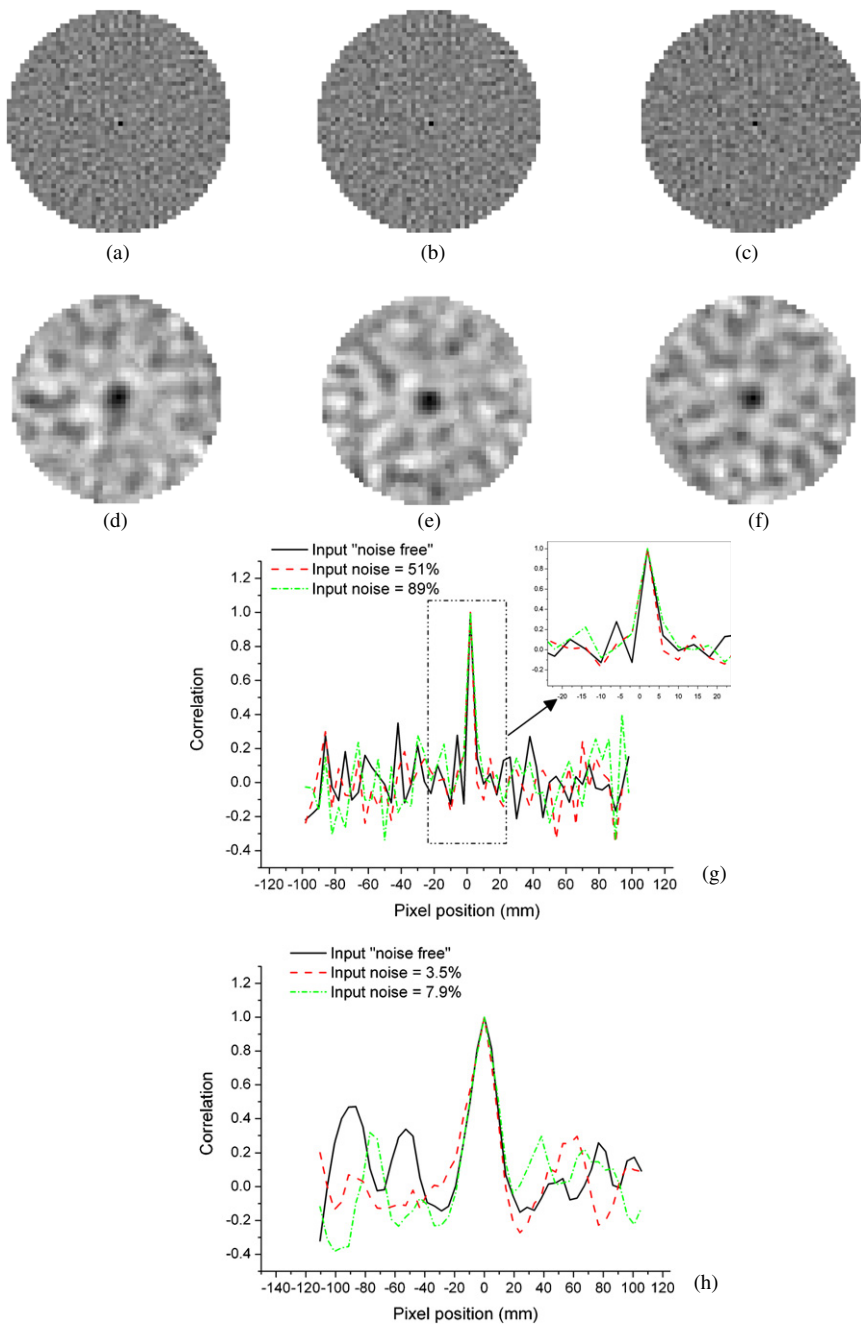


Figure 6. Correlation images for the central voxel of the central transaxial slice and corresponding profiles across the images. Correlation images in PET with (a) 'noise-free' INPUT, (b) 51% of INPUT noise and (c) 89% of INPUT noise. Correlation images in SPECT with (d) 'noise-free' INPUT, (e) 3.5% of INPUT noise and (f) 7.9% of INPUT noise. Horizontal profiles through the centre of the images are shown in (g) for PET and (h) for SPECT.

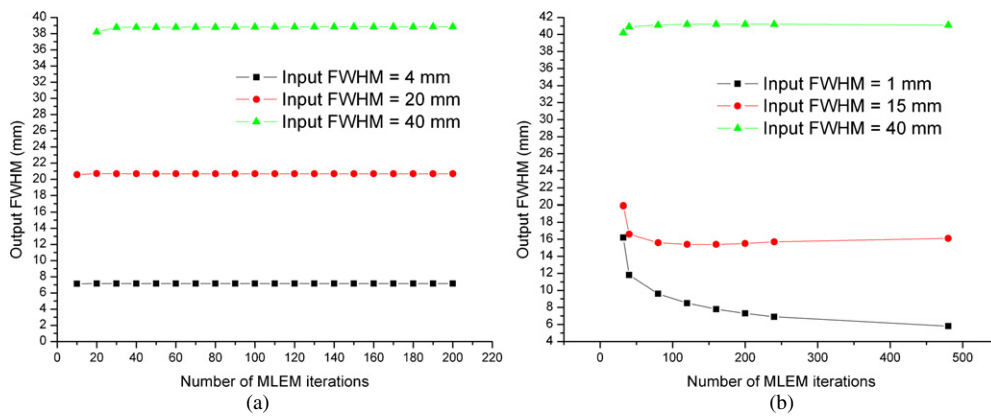


Figure 7. Convergence of the reconstructed FWHM for various INPUT spatial resolutions: (a) PET case and (b) SPECT case.

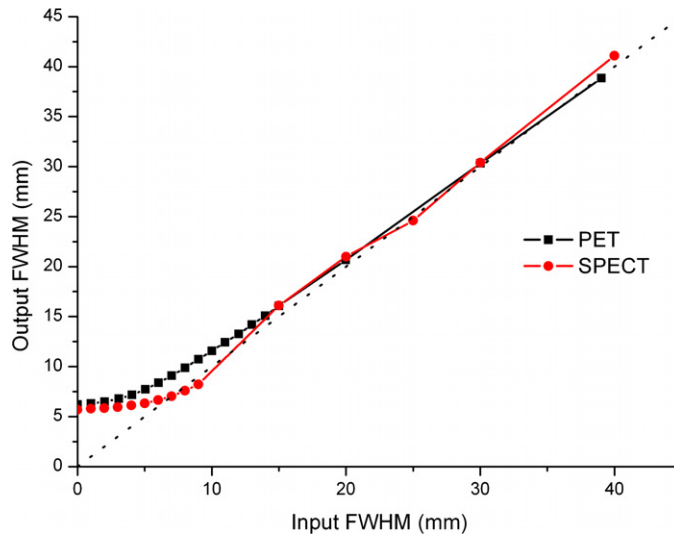


Figure 8. Variation of the OUTPUT spatial resolution as a function of the INPUT spatial resolution for the PET and SPECT cases. The dotted line is the identity line.

Indeed, unlike the PET reconstruction algorithm, the SPECT Flash3D algorithm included 3D resolution modelling (details on implementation not known).

3.3. Simulations of real patient scans

3.3.1. PET case. Figure 9 shows the patient PET images reconstructed for the different spatial resolution/noise compromises in the INPUT data (see section 2.3.1). Associated profiles show that the reconstructed volumes resulting from the high-noise and high-resolution PET image ($R_H N_H$) or from the medium-noise and medium-resolution image ($R_M N_M$) are most similar to the acquired scan. Visual assessment shows that all OUTPUT images have about the same level of noise, confirming that there is no substantial propagation of the INPUT noise during the simulation/reconstruction process.

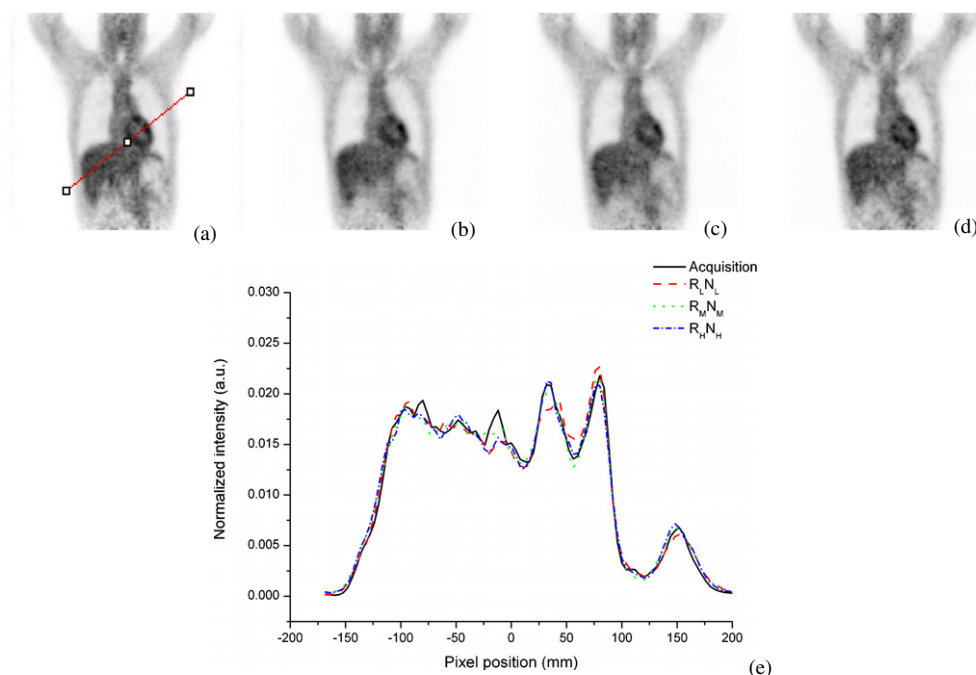


Figure 9. Patient PET images reconstructed from (a) the acquired sinogram, (b) the sinogram simulated from the $R_L N_L$ INPUT image, (c) the sinogram simulated from the $R_M N_M$ INPUT image and (d) the sinogram simulated from the $R_H N_H$ INPUT image. All grey scales are identical. The red line in (a) shows the position of the profile drawn through the different images (e). Profiles were normalized to the same area under the curve.

3.3.2. *SPECT case.* Figure 10 shows the patient SPECT images reconstructed for the different spatial resolution/noise compromises in the INPUT data (see section 2.3.2). Profiles through the images (figure 10(e)) confirm that the reconstructed volumes obtained when using the $R_H N_H$ or $R_M N_M$ activity maps as an INPUT for the simulation were most similar to the reconstructed clinical scan. Again, the noise level did not propagate substantially through the simulation and reconstruction process: there is no more noise in (d) than in (c) or (b).

4. Discussion

MC simulations of highly realistic scans are needed to evaluate quantification methods under conditions close to those encountered in a clinical setting (Buvat and Castiglioni 2002). In this study, we determined what the noise and spatial resolution of the activity map used as an input of the simulation should be, to obtain simulated PET/SPECT images indistinguishable from real patient scans for ^{131}I SPECT and ^{18}F -FDG PET.

4.1. Noise in the INPUT activity map

To study the propagation of the noise present in the INPUT activity map through the simulation/reconstruction process, we used a noise FOM derived from a single slice instead of using multiple independent realizations of noise. The reason for extracting only one slice was to avoid the variation of the noise level along the axial direction in PET, due to the variation of

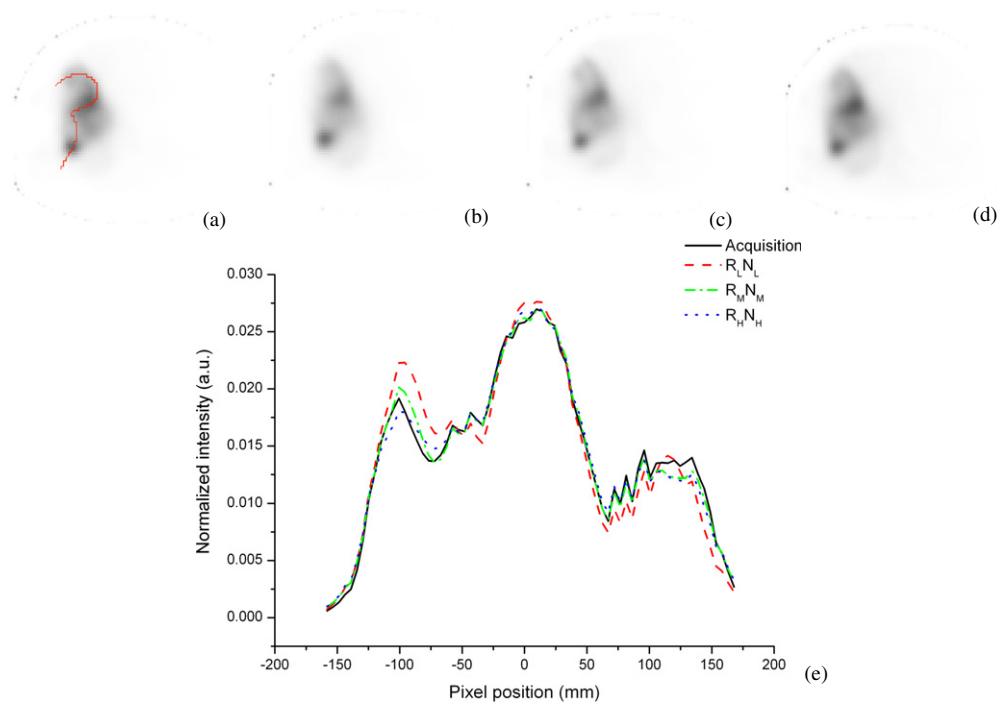


Figure 10. SPECT images reconstructed from (a) the acquired sinogram, (b) the sinogram simulated from the $R_L N_L$ INPUT image, (c) the sinogram simulated from the $R_M N_M$ INPUT image and (d) the sinogram simulated from the $R_H N_H$ INPUT image. All grey scales are identical. The red line in (a) shows the position of the profile drawn through the different images (e). The profile does not correspond to a straight line to better go through the different foci of activity. Profiles were normalized to the same area under the curve.

axial sensitivity in PET. The number of independent realizations ('PIXEL noise' method) was equal to the number of voxels in a specific ROI ('ROI noise' method). The number of ROIs was also equal to the number of voxels considered within the slice ('PIXEL noise' method). By doing so, the statistical power was the same in the two methods used to characterize the noise. Moreover, the noise correlation study shows that the ROIs (hence, the central pixel inside these ROIs) were far apart to avoid any correlation between them. The pixels used for the noise study could thus be considered as independent. As already shown by Tong *et al* (2010) and Schmidtlein *et al* (2010), we found that our 'ROI noise' was an accurate estimate of the reference 'PIXEL noise' that would be obtained using a much more computationally demanding approach.

Based on our noise FOM, an important finding was that, from a certain level of noise in the INPUT activity maps, the noise in the images reconstructed from the simulated data was almost independent of the noise in the input activity map, both for the PET and SPECT data. Given that the Flash3D algorithm was limited to 480 equivalent MLEM iterations and that it included some regularization that prevented us from obtaining images with high noise level, we could not investigate a range of INPUT noise as large as that investigated in PET, but the trends regarding the variation of the OUTPUT noise as a function of the level of INPUT noise were similar. The correlation images obtained for the SPECT data presented a smoother variation (hence, a higher correlation) than for the PET data (figure 6), consistent

with a high spatial regularization embedded in the SPECT Flash3D reconstruction involving resolution modelling. The very small correlation in PET images can be explained by the use of the Siddon method (Siddon 1985) in the forward and backward projection steps of the reconstruction algorithm. This method uses the line integral model without any interpolation, so the number of voxels contributing to a given line-of-response is small, thus introducing few correlations between them. Other commonly used projectors like the ones described by Herman (1980) or Joseph (1983) would have involved more voxels in a given line-of-response as they use interpolations, and thus would introduce more noise correlation.

The fact that a large noise present in the INPUT activity maps does not propagate through the simulation process can be explained as follows. First, the noise present in our INPUT activity maps mostly results from an over-fit of the noisy projections when many MLEM iterations are used (Veklerov and Llacer 1987). Yet, whatever the noise level in these reconstructed images, they are still consistent with the measured projections, based on the statistical model underlying MLEM, and the noise in their projections is less than or equal to the one originally present in the measured data. Second, a MC simulation can be seen as a highly realistic noisy forward projector, combining a geometric projection (acting as the Siddon projector) and a stochastic blurring process (due to finite crystal size, crystal penetration and scattering, collimator fluorescence in SPECT, etc). Therefore, when performing a MC simulation using a noisy image as the INPUT activity distribution, and for an infinite number of emitted particles, the MC simulated projections have less noise than the projections that would be obtained by just ray tracing, because the stochastic blurring smoothes the noise in neighbouring projection bins. When simulating an acquisition of duration similar to that used in clinical routine, the noise level inherent to the MC simulation approach is higher than the remaining noise related to the stochastic blurring. So, the final noise level in the simulated projections is dominated by the noise level expected for the simulated acquisition duration, and not by the noise present in the initial activity map. This is why there is no noise amplification through the MC simulation/reconstruction process, provided the noise initially present in the acquired projections is not dominant.

4.2. Spatial resolution in the INPUT activity map

Figure 8 suggests that for INPUT spatial resolutions lower than 15 mm, the relationship between INPUT and OUTPUT spatial resolutions is no longer linear. This is because there is an inevitable loss of resolution due to the modelling of the scanner spatial response in the simulations. When the spatial resolution in the INPUT image is larger than the spatial resolution degradation due to the imaging process, this loss is expected to be negligible. The unavoidable loss of resolution can be seen on the y-axis in figure 8 for a null INPUT spatial resolution (i.e. point source without blurring). The SPECT OUTPUT spatial resolutions are lower than PET ones. This is because of the 3D resolution modelling in the SPECT reconstruction algorithm, unlike in the PET reconstruction. An important conclusion is that an OUTPUT spatial resolution similar to that observed in clinical images can be obtained for both PET and SPECT, provided the best possible INPUT spatial resolution is used (as obtained at high iteration number). Indeed, real clinical scans usually have a spatial resolution that is not the highest achievable by the tomograph, because such high resolution would result in images that would be too noisy to be interpreted clinically. As a result, the spatial resolution of clinical whole-body PET scans is usually not better than 6–7 mm. Figure 8 shows that such output resolution can be achieved when using images with about 5 mm input resolution. This latter resolution is achievable in PET using a high number of iterations (never used in the clinic). The same reasoning holds for SPECT: clinical SPECT images with a typical resolution

of 8–10 mm can be simulated using input images with a resolution of 7–8 mm, which can be obtained using a high iteration number.

4.3. Recommendations and limitations

Our results suggest that highly realistic simulated images indistinguishable from real scans can be obtained when using an activity map derived from patient images reconstructed with a higher than usual number of iterations. This was confirmed visually by simulating real patient ^{18}F -FDG PET and ^{131}I SPECT scans (figures 9 and 10). Subtle differences between the volumes reconstructed with the $R_M N_M$ and the $R_H N_H$ INPUT data suggest that a very high level of noise might impact some small structures in heterogeneous activity distributions.

The spatial resolution was assessed using a simple FOM: a 2D transaxial Gaussian fit of the near-central impulse response function. A more complete evaluation could account for the 3D components of the spatial resolution in air and in presence of scattering medium. However, we believe that the conclusions drawn with our simple FOM are valid to describe the link between the INPUT and OUTPUT spatial resolutions.

Only high-energy SPECT (^{131}I) and ^{18}F PET simulations were investigated in our study. Other radionuclides would yield different compromises between spatial resolution and noise, due to different energy and collimator features in SPECT, and to different mean-free paths of the emitted positrons in PET. Although we came to similar conclusions regarding the propagation of the noise and spatial resolution during the simulation/reconstruction process in very different settings (^{131}I SPECT and ^{18}F -FDG PET), the applicability of these conclusions to other radionuclides still deserve to be confirmed. Yet, in PET, no radionuclide dependence is expected as long as only the annihilation position is simulated and the positron mean-free path is not corrected for in the reconstructed images, so that INPUT activity maps and reconstructed images are consistent (both mapping annihilation positions).

All the results obtained in this study hold for iterative algorithms. Extrapolation to analytical reconstruction like the 2D or 3D reprojection filtered backprojection might need further investigation. Also, we studied only MC simulations because the basic aim was to simulate highly realistic clinical images. Similar conclusions were previously reported using analytical simulations only (Barnden and Hutton 2006).

5. Conclusion and future work

We demonstrated that highly realistic patient SPECT and PET images could be simulated using MC simulations and input activity maps with appropriate spatial resolution and noise level. Our results show that spatial resolution in the input activity map has to be carefully chosen, favouring activity maps with spatial resolution higher than usually used in the clinics, to produce reconstructed images undistinguishable from clinical ones. The increased noise associated with high-resolution activity maps does not propagate through the simulation/reconstruction process, making it possible to simulate images with the same spatial resolution and noise as that used in the clinical routine.

Acknowledgments

This work was funded in part by ANR grant no ANR-06-CIS-2004. UCL/UCLH receives a portion of research support from the UK Department of Health's Biomedical Research Centres funding scheme.

References

- Bailey D L and Meikle S R 1994 A convolution-subtraction scatter correction method for 3D PET *Phys. Med. Biol.* **39** 411–24
- Barnden L and Hutton B 2006 Preliminary assessment of the use of patient images as input models in Monte Carlo simulations *J. Nucl. Med.* **47** (Suppl. 1) 49
- Barrett H H, Wilson D W and Tsui B M 1994 Noise properties of the EM algorithm: theory *Phys. Med. Biol.* **39** 833–46
- Buvat I and Castiglioni I 2002 Monte Carlo simulations in SPET and PET *Q. J. Nucl. Med.* **46** 48–61
- Carlier T, Descourt P, Maigne L, Visvikis D, Bardies M and Buvat I 2009 Efficient simulations of iodine 131 SPECT scans using GATE *IEEE Nucl. Sci. Symp. Conf. Rec.* pp 3412–14
- Descourt P, Carlier T, Du Y, Song X, Buvat I, Frey E C, Bardies M, Tsui B M W and Visvikis D 2010 Implementation of angular response function modelling in SPECT simulations with GATE *Phys. Med. Biol.* **55** N253–66
- Herman G T 1980 *Image Reconstruction from Projections: The Fundamentals of Computerized Tomography* (New York: Academic) p 63
- Jan S *et al* (for the OpenGATE collaboration) 2004 GATE: a simulation toolkit for PET and SPECT *Phys. Med. Biol.* **49** 4543–61
- Jan S *et al* (for the OpenGATE collaboration) 2011 GATEV6: a major enhancement of the GATE simulation platform enabling modelling of CT and radiotherapy *Phys. Med. Biol.* **56** 881–901
- Joseph P 1983 An improved algorithm for reprojecting rays through pixel images *IEEE Trans. Med. Imaging* **1** 192–6
- Kadrmas D J 2004 LOR-OSEM: statistical PET reconstruction from raw line-of-response histograms *Phys. Med. Biol.* **49** 4731–44
- Lamare F, Turzo A, Bizais Y, Cheze Le Rest C and Visvikis D 2006 Validation of a Monte Carlo simulation of the Philips Allegro/GEMINI PET systems using GATE *Phys. Med. Biol.* **51** 943–62
- Le Maitre A, Segars W P, Marache S, Reilhac A, Hatt M, Tomei S, Lartizien C and Visvikis D 2009 Incorporating patient-specific variability in the simulation of realistic whole-body 18F-FDG distributions for oncology applications *IEEE Proc.* **97** 2026–38
- Politte D G and Snyder D L 1991 Corrections for accidental coincidences and attenuation in maximum-likelihood image reconstruction for positron-emission tomography *IEEE Trans. Med. Imaging* **10** 82–9
- Rehfeld N S, Stute S, Apostolakis J, Soret M and Buvat I 2009 Introducing improved voxel navigation and fictitious interaction tracking in GATE for enhanced efficiency *Phys. Med. Biol.* **54** 2163–78
- Schmidtlein C R, Beattie B J, Bailey D L, Akhurst T J, Wang W, Gönen M, Kirov A S and Humm J L 2010 Using an external gating signal to estimate noise in PET with an emphasis on tracer avid tumors *Phys. Med. Biol.* **55** 6299–326
- Segars W P and Tsui B M W 2009 MCAT to XCAT: the evolution of 4-D computerized phantoms for imaging research *Proc. IEEE* **97** 1954–68
- Shepp L A and Vardi Y 1982 Maximum likelihood reconstruction for emission tomography *IEEE Trans. Med. Imaging* **1** 113–22
- Siddon R L 1985 Fast calculation of the exact radiological path for a three-dimensional CT array *Med. Phys.* **12** 252–5
- Stute S, Benoit D, Martineau A, Rehfeld N S and Buvat I 2011 A method for accurate modelling of the crystal response function at a crystal sub-level applied to PET reconstruction *Phys. Med. Biol.* **56** 793–809
- Stute S, Tylski P, Grotus N and Buvat I 2008 LuCaS: efficient Monte Carlo simulations of highly realistic PET tumor images *IEEE Nucl. Sci. Symp. Conf. Rec.* pp 4010–12
- Sureau F C, Reader A J, Comtat C, Leroy C, Ribeiro M J, Buvat I and Trébossen R 2008 Impact of image-space resolution modeling for studies with the high-resolution research tomograph *J. Nucl. Med.* **49** 1000–8
- Tomei S, Reilhac A, Visvikis D, Boussion N, Odet C, Giammarile F and Lartizien C 2010 OncoPET_DB: a freely distributed database of realistic simulated whole body 18F-FDG PET images for oncology *IEEE Trans. Nucl. Sci.* **57** 246–55
- Tong S, Alessio A M and Kinahan P E 2010 Noise and signal properties in PSF-based fully 3D PET image reconstruction: an experimental evaluation *Phys. Med. Biol.* **55** 1453–73
- Veklerov E and Llacer J 1987 Stopping rule for the MLE algorithm based on statistical hypothesis testing *IEEE Trans. Med. Imaging* **6** 313–9
- Vija A H, Hawman E G and Engdahl J C 2004 Analysis of a SPECT OSEM reconstruction method with 3D beam modelling and optional attenuation correction: phantom studies *IEEE Nucl. Sci. Symp. Conf. Rec.* pp 2662–6